Journal of Catalysis 263 (2009) 335–344

Contents lists available at ScienceDirect

Journal of Catalysis

www.elsevier.com/locate/jcat

The effects of CeO_2 on the activity and stability of Pt supported catalysts for methane reforming, as addressed by *in situ* temperature resolved XAFS and TEM analysis

A.P. Ferreira [a], D. Zanchet [b], J.C.S. Araújo [a], J.W.C. Liberatori [a], E.F. Souza-Aguiar [d], F.B. Noronha [c], J.M.C. Bueno [a,*]

[a] *Universidade Federal de São Carlos-UFSCar, Cx. P. 676, São Carlos, SP, Brazil*
[b] *Laboratório Nacional de Luz Síncrotron-LNLS, Cx. P. 6192, 13083-970, Campinas, SP, Brazil*
[c] *Laboratório de Catálise, Instituto Nacional de Tecnologia, Av. Venezuela, 82/518, Centro, 21081-312, Rio de Janeiro, RJ, Brazil*
[d] *Universidade Federal do Rio de Janeiro, CENPES/PETROBRAS, Rio de Janeiro, RJ, Brazil*

ARTICLE INFO

Article history:
Received 3 December 2008
Revised 20 February 2009
Accepted 23 February 2009
Available online 17 March 2009

Keywords:
CeO_2
Pt-supported catalysts
Synthesis gas
Natural gas
Autothermal reforming of methane
Partial oxidation of methane
In situ XAFS

ABSTRACT

The effects of Ce as a promoter on the activity and stability of Pt/Al_2O_3 and Pt/CeO_2–Al_2O_3 catalysts for autothermal reforming and partial oxidation of methane (POM) were investigated. The Pt/CeO_2–Al_2O_3 catalyst exhibited higher activity and stability than the Pt/Al_2O_3 catalyst. Analysis by *in situ* X-ray absorption spectroscopy under POM conditions reveals that Pt is reduced by heating the catalysts to about 730 K. The overall first-shell coordination numbers suggest changes in Pt cluster morphology with increasing temperature. Transmission electron microscopy showed strong Pt agglomeration with time on stream for the Pt/Al_2O_3 catalyst. The higher stability of the Pt/CeO_2–Al_2O_3 catalyst was attributed to a combination of different properties: (i) hindrance of carbon deposition on the Pt surface for a reactor fed with low H_2O/CH_4 ratio; (ii) interaction of Pt–O–Ce species in the presence of oxygen, inhibiting vapor and diffusion transport of PtO_2 and mainly, (iii) thermal stability of the support, which prevents the loss of surface area, and consequently the sintering of the Pt.

1. Introduction

Recently, the need to reduce dependence on petroleum feedstocks and the continuous increase of known natural gas reserves have generated great interest in the conversion of natural gas to fuels and petrochemical products. Although in the near future there is need to change towards bio- and renewable chemical sources, the dependence on fossil fuel will continue for many years. The development of new efficient catalytic processes to produce cleaner fuels is a challenge to environmental requirements. The so-called gas-to-liquids (GTL) technology, which deals with the conversion of natural gas to fuels and petrochemical products, is a promising solution for the exploitation of stranded gas reserves and promises to produce sulfur-free synfuels. In this technology, the production of the synthesis gas (CO and H_2) represents a step of major importance and represents half of the capital cost of the GTL plant [1]. Autothermal reforming (ATR) technology is the preferred option to produce synthesis gas with H_2/CO ratio equal to 2, which is suitable for subsequent use in the Fischer–Tropsch synthesis [2]. In ATR technology, the H_2/CO ratio can be modified by adjusting the composition of the reactant mixture, CH_4:H_2O:O_2, and a low ratio of steam/carbon is required to obtain a H_2/CO ratio around 2.

Recently, Jones et al. [3] showed that Ru and Rh are the most active pure transition metals for methane steam reforming, while supported Ni, Ir, Pt, and Pd catalysts are significantly less active at similar dispersions. Other authors demonstrated that these reforming reactions occur on supported metal (Ni, Pt, Ir and Ru) catalysts, that the activity of polycrystalline catalysts increases with the metal dispersion and that supported Pt catalysts show the highest activity [4,5]. The reaction rates are limited exclusively by C–H bond activation on metal cluster surfaces and the co-reactant activation is not kinetically relevant [4]. This indicates that the chemical state and morphology of the Pt surface are important to determine the activity.

The thermodynamics of methane reforming reactions demand elevated temperatures (~1073 K or above) to obtain high methane conversion and, under these conditions, metal agglomeration is favored, leading to a decrease in activity with time on stream. At high temperatures, the decomposition of methane occurs through successive steps of dissociation of CH_4, producing C^* species ($CH_4 \rightarrow C^* + 2H_2$) and the disproportionation of CO at low temperature ($2CO \rightarrow C^* + CO_2$) [3–6]. Under low steam/carbon ratio conditions, required in ATR processes to obtain a H_2/CO ratio around 2, the reaction rates can be un-equilibrated and decrease

* Corresponding author. Fax: +55 16 33518466.
E-mail address: jmcb@ufscar.br (J.M.C. Bueno).

0021-9517/$ – see front matter
doi:10.1016/j.jcat.2009.02.026

carbon removal ($C^* + O^* \leftrightarrow CO^* + *$) can result in carbon accumulation on the metal surface.

Becker et al. [7] reported that an oxygen-rich surface of alumina-supported Pt catalysts seems to hinder the dissociative adsorption of methane, leading to a low methane oxidation activity. Recently, Nagai et al. [8] reported that Pt did not sinter after aging treatment at 1073 K in air on a Pt/ceria-based oxide catalyst, while sintering occurs on a Pt/Al_2O_3 catalyst. Based on X-ray absorption spectroscopy experiments, they concluded that Pt sintering could be inhibited by the Pt-oxide–support interaction.

The activity and stability of catalysts for methane reforming are also strongly influenced by the support and metal dispersion [9–11], and Pt/ceria-based oxide catalysts exhibit the highest activity and stability [9,12,13]. Thus, many parameters such as Pt dispersion, composition of support, composition of reactant and temperature of reaction can affect the stability and activity of catalysts in reactions of methane reforming.

We have previously reported the effects of CeO_2 loading on the properties and catalytic behavior of CeO_2–Al_2O_3-supported Pt catalysts on dry reforming and partial oxidation of methane [9,13] and those catalysts with 12 wt% of CeO_2 showed the highest catalytic activity and stability.

To elucidate the influence of Ce on the stability and activity of Pt supported catalysts for methane reforming, we present results obtained by *in situ* temperature-resolved X-ray absorption near-edge structure (XANES) spectroscopy of CeO_2–Al_2O_3-supported Pt catalysts under POM conditions, extended X-ray absorption fine-structure (EXAFS) of reduced catalysts and transmission electron microscopy (TEM) of fresh and used catalysts. The higher TOF_{CH_4} observed for Pt/CeO_2–Al_2O_3 than Pt/Al_2O_3 catalyst is attributed to higher capacity to transfer O* from support to Pt sites, which leads to oxidation of carbon and a higher accessibility of the active sites to CH_4 and consequently to higher TOF_{CH_4}. The interaction of Pt with the support and morphology of Pt was understood and the higher stability of the Pt/CeO_2–Al_2O_3 catalyst could be attributed to the interaction of Pt and Ce in presence of oxygen and, mainly, to the thermal stability of the support, which prevents the sintering of the Pt clusters.

2. Experimental

2.1. Catalyst preparation

$12CeO_2$–Al_2O_3 supports containing 12 wt% of CeO_2 were prepared by incipient wetness impregnation of γ-Al_2O_3 (Engelhard, $S_{BET} = 205\ m^2\ g^{-1}$), previously calcined at 773 K, with an aqueous solution of $(NH_4)_2[Ce(NO_3)_6]$ (99.99% Aldrich) [9]. After impregnation, the supports were calcined at 773 K for 8 h.

Pt/Al_2O_3 and $Pt/12CeO_2$–Al_2O_3 catalysts were prepared by impregnation of the respective support with a solution of $H_2PtCl_6 \cdot 6H_2O$ (Degussa) in ethanol. The mixture was stirred for 2 h at room temperature and the solvent was removed using a Rotavapor at 343 K. The samples were dried at 343 K overnight. For all samples, the amount of Pt was about 1 wt% and they were referred as Pt/A, in the case of Pt/Al_2O_3, and Pt/CA, in the case of $Pt/12CeO_2$–Al_2O_3.

Pt/A and Pt/CA samples after impregnation (precursors) were treated at different temperatures and atmosphere conditions: (i) precursors treated in air for 8 h at low temperature (773 K) were named Pt/A-O2-L and Pt/CA-O2-L; (ii) precursors treated in air at high temperature (1073 K) for 24 h were named Pt/A-O2-H and Pt/CA-O2-H; (iii) Pt/A-O2-L and Pt/CA-O2-L samples reduced in H_2 at low temperature (773 K) for 1 h were named Pt/A-H2-L and Pt/CA-H2-L; (iv) Pt/A-O2-L and Pt/CA-O2-L samples reduced in H_2 at high temperature (1073 K) for 24 h were named Pt/A-H2-H and Pt/CA-H2-H.

2.2. Characterization

Chemical analyses of the samples obtained by inductively coupled plasma–atomic emission spectroscopy were carried out using an AtomScan 25 spectrometer (Thermo Jarrel Ash).

X-ray diffraction (XRD) patterns were collected with a Rigaku DMAX 2500 PC diffractometer using CuK_α radiation with a Ni filter, 2θ from 5 to 80° with step-size of 0.02° and counting time of 2 s. The apparent crystallite sizes of the Pt and CeO_2 were determined using Scherrer's equation.

Temperature-programmed reduction (TPR) profiles were recorded on a Micromeritics Pulse Chemisorb 2705. Prior reduction, 0.150 g of sample was pre-treated at 423 K in a N_2 stream for 1 h and cooling to room temperature. TPR was carried out by heating the sample at 10 K min^{-1} from room temperature to 1273 K, under a flow mixture containing 5% H_2/Ar (30 mL min^{-1}). H_2 consumption was measured using a thermal conductivity detector.

Pt/A-O2-L and Pt/CA-O2-L were also submitted to different reduction–oxidation cycles: (i) Cycle 1—after undergoing TPR, Pt/A-O2-L and Pt/CA-O2-L samples were heated under synthetic air flow (20 mL min^{-1}) at 5 K min^{-1} to 1073 K, holding for 1 h; after cooling, another TPR was performed. (ii) Cycle 2—after cycle 1 and TPR, the samples were heated under synthetic air flow (20 mL min^{-1}) at 5 K min^{-1} to 1073 K, holding for 8 h; after cooling, another TPR was performed.

Pt/A-H2-L and Pt/CA-H2-L samples were used in ATR reaction for 24 h. These fresh and used samples were investigated by TEM using a JEM 3010 microscope, operating at 300 kV (1.7 Å point resolution) at the LME-Brazilian Synchrotron Light Laboratory (LNLS), in Campinas-SP, Brazil. The samples were suspended in isopropanol and dropped on an amorphous carbon coated copper grid for the TEM analysis.

XANES spectra at the Pt L_3-edge (11,564 eV) were measured at the D06A-DXAS beamline of the LNLS. The D06A-DXAS is a dispersive beamline equipped with a focusing curved Si(111) monochromator, operating in Bragg mode, that selects the X-ray energy bandwidth (11,400–12,000 eV), and with a 1152 × 1242 (500 × 900) pixel CCD solid-state detector that converts X-rays into visible light for spectral analysis. The samples were prepared as self-supporting pellets and placed into a tubular quartz furnace (diameter = 20 mm and X-ray path length = 440 mm) that was sealed with kapton refrigerated windows for the transmission measurements. XANES spectra at the Pt L_3-edge were collected *in situ* at different temperatures and atmospheres. Temperature-resolved XANES-H_2 spectra were acquired during TPR of Pt/A-O2-L and Pt/CA-O2-L samples under H_2:He flow (5:95) up to 773 K (total flow: 100 mL min^{-1}, corresponding to a space velocity around 70,000 h^{-1}, rate: 10 K min^{-1}, holding time: 1 h), and during the cooling down of the reduced sample to room temperature. Temperature-resolved XANES-POM spectra were acquired during heating of the reduced Pt/A-H2-L and Pt/CA-H2-L samples up to 973 K under a POM reaction mixture containing CH_4:O_2 at the ratio of 2:1 diluted in He (total flow: 100 mL min^{-1}, rate: 5 K min^{-1}, holding time: 30 min at 573, 673, 773 and 973 K).

EXAFS measurements at the Pt L_3-edge were carried out at the D04B-XAFS1 beamline of the LNLS. This beamline is equipped with a (111) silicon channel-cut and the measurements were performed in transmission mode, with the same furnace used in the XANES measurements. Athena/Artemis software packages [14] were used to extract the EXAFS signal from the measured absorption spectra using standard proceedings [15]. The EXAFS oscillations were fitted in R-space using k^2-weighted Fourier filtering, taking into account the anharmonicity of the pair-potentials by utilizing the third cumulate in the analysis. EXAFS data for the Pt catalysts were fitted considering Pt–Pt and Pt–O contributions, $R = 1.0$–3.2 Å, Kaiser–Bessel window, and backscattering amplitudes calculated with the

FEFF6 code. The theoretical references were calibrated with the experimental EXAFS data for Pt-foil.

2.3. Catalytic test

2.3.1. Activity measurements

CH_4 turnover rates (TOF_{CH_4}) in steam reforming were measured in a fixed bed quartz reactor (i.d. 8 mm) as previously described by Araujo et al. [11]. The reactions were carried out under atmospheric pressure using catalyst powders (100 mg; 80–100 mesh particles) diluted with quartz beads (300 mg) with similar granulometry. The samples were reduced at 773 K, for 1 h under H_2 flow of 30 mL min^{-1}. Feed composition was 1:3:0.5 $CH_4/H_2O/N_2$ at a total flow-rate of 2–4 $\times 10^{-3}$ mol s^{-1}. TOF_{CH_4} at 773 K was calculated from the specific reaction rate and using the Pt dispersion determined from cyclohexane dehydrogenation rate, as previously described by Santos et al. [9].

The stability of Pt/A and Pt/CA catalysts were evaluated for ratios of reactants H_2O:O_2:CH_4 corresponding to ATR and POM reactions. The experiments were performed in a fixed-bed quartz reactor with inner diameter of 8 mm and a thermocouple with a diameter of 1.8 mm mounted inside the reactor at atmospheric pressure. In order to avoid hot spot formation, catalyst samples (40 mg) were diluted with inert SiC (72 mg). The Pt/A-O2-L and Pt/CA-O2-L samples were reduced *in situ* at 773 K for 1 h, under H_2 flow of 30 mL min^{-1} and then heated up to 1073 K under N_2. The catalyst stability was tested for 24 h on stream at 1073 K in CH_4 reforming reactions with various reactant molar ratios (H_2O:O_2:CH_4), such as $CH_4/O_2 = 2$ and $H_2O/CH_4 = 0.0$, 0.2 and 0.64. The total flow rate of CH_4 and O_2 was 100 mL min^{-1}.

The reactants and products were analyzed using a gas chromatograph (Varian 3800) equipped with a thermal conductivity detector and a CP-carboplot column (Chrompack), as previously described in [9].

3. Results

3.1. Catalyst preparation and characterization

Pt/A and Pt/CA catalysts had Pt loadings of 1.00 ± 0.05 wt%. Textural properties of Pt/A-H2-L and Pt/CA-H2-L catalysts were previously reported by Santos et al. [9], with surface areas (S_{BET}) of 76 and 72 m^2 g^{-1}, respectively. Pt dispersions, calculated from the data of cyclohexane dehydrogenation rate at 543 K, were 66% for Pt/A-H2-L and 54% for Pt/CA-H2-L.

XRD patterns of the Pt/A-H2-L and Pt/CA-H2-L catalysts are shown in Fig. 1, curves (a) and (c), respectively. These samples did not show clearly the diffraction lines characteristic of metallic Pt ($2\theta = 39.9$ and 47.0°). Pt/A-H2-H and Pt/CA-H2-H samples (data not shown), presented XRD patterns similar to those of the respective samples reduced at low temperature (Pt/A-H2-L and Pt/CA-H2-L). These results suggest that Pt is well dispersed and there is no agglomeration of Pt particles after reduction at high temperature (1073 K).

On the other hand, Pt/A-O2-H and Pt/CA-O2-H catalysts, clearly showed the diffraction lines of metallic Pt (Fig. 1, curves b and d). The apparent crystalline particle size of Pt, obtained by the Scherrer's equation, was about 30 nm for both samples (Table 1). These results reveal an increase of the Pt particle sizes when treated in air.

The diffraction lines of CeO_2 fluorite structure at $2\theta = 28.5$, 33.3, 47.5 and 56.4° (curve e) were clearly observed for the Pt/CA-O2-L and Pt/CA-O2-H samples, and the CeO_2 particle sizes were 16 and 28 nm, respectively (Table 1). These results showed the crystallization of CeO_2 when treated in air and particle growth with the increase of the temperature.

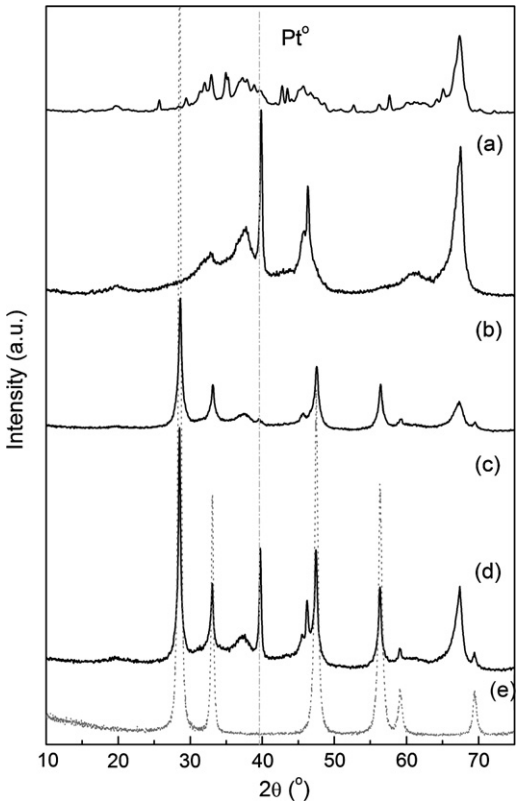

Fig. 1. XRD patterns of the catalysts: (a) Pt/A-H2-L; (b) Pt/A-O2-H; (c) Pt/CA-H2-L; (d) Pt/CA-O2-H; (e) CeO_2 reference. The dashed line indicates the 111 peak position of Pt^0 ($2\theta = 39.9°$).

Table 1
Pt and CeO_2 particle size (D_{XRD}) and H_2 total uptake and relative consumption (reduction of Pt oxides species) of the fresh catalysts and after redox cycles.

Catalysts	Pt D_{XRD} (nm)	CeO_2 D_{XRD} (nm)	H_2 (μmol g_{cat}^{-1}) $\times 10^{-5}$	H_2 (μmol g_{Pt}^{-1}) $\times 10^3$
Pt/A-O2-L	–	–	1.2	1.0
Pt/A-O2-H	31	–	–	–
Pt/A-O2-L (cycle 1)	21	–	–	–
Pt/A-O2-L (cycle 2)	21	–	–	–
Pt/CA-O2-L	–	16	3.9	2.1
Pt/CA-O2-H	30	28	–	–
Pt/CA-O2-L (cycle 1)	17	19	3.9	0.8
Pt/CA-O2-L (cycle 2)	18	18	2.7	0.7

Fig. 2 shows TPR profiles for the Pt/A-O2-L and Pt/CA-O2-L samples and after redox cycles 1 and 2. The Pt/A-O2-L sample (Fig. 2A, a) shows the main peak at 576 K and minor peaks at 500 and 685 K whereas the Pt/CA-O2-L shows the main peak at lower temperature (480 K). It has been shown that $PtCl_6^{2-}$ species on Al_2O_3 surface are reduced at 390 K whereas oxychlorinated species (PtO_xCl_y) are reduced at higher temperature, which depends on the thermal treatment of the sample [16]. As a consequence, these results suggest the presence of oxychlorinated species in both catalysts. H_2 consumption is shown in Table 1. In the case of Pt/CA-O2-L, the value is higher than the one expected for the Pt^{4+} contents, indicating that the superficial ceria is also reduced [13]. The H_2 uptake around 950–1050 K in the Pt/CA-O2-L was ascribed to the reduction of the $CeAlO_3$ precursor and bulk ceria crystallites [17,18].

The reduction profiles of Pt/A-O2-L, before and after cycle 1 (Fig. 2A, a and b), show a drastic reduction of H_2 consumption. After the second redox treatment (cycle 2, Fig. 2A, c), H_2 consumption could no longer be detected. XRD patterns of these two

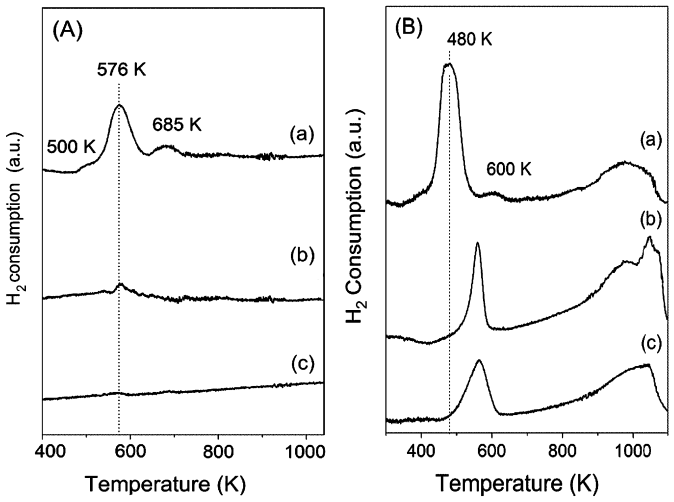

Fig. 2. TPR profiles of Pt/A-O2-L (A, a) and Pt/CA-O2-L (B, a); after redox cycle 1: Pt/A-O2-L (A, b), Pt/CA-O2-L (B, b); and after redox cycle 2: Pt/A-O2-L (A, c) and Pt/CA-O2-L (B, c).

samples (not shown) presented intense diffraction lines of metallic Pt ($2\theta = 39.9°$), with particle sizes around 21 nm (Table 1). These results confirm Pt growth that could be related to surface diffusion and vapor phase transport of PtO_x, during the heating under air at high temperature.

In the case of the Pt/CA-O2-L (Fig. 2B, a and b), after cycle 1 the consumption of H_2 at low temperature decreases and the main peak shifts from 480 to 580 K. At high temperature, there is an increase of the relative intensity of the peak at 1050 K. The TPR analysis after cycle 2 (Fig. 2B, c) shows similar profile, but with low H_2 consumption (Table 1). The changes in the peak shape at high temperature indicate the dispersion and agglomeration of ceria due to the redox treatment [19]. XRD patterns (not shown) confirmed the presence of metallic Pt after both cycles, with particle sizes of 17 nm (cycle 1) and 18 nm (cycle 2), Table 1. From these results, it is reasonable to propose that in the Pt/CA-O2-L sample, Pt and superficial ceria are reduced at similar temperature around 480 K and after cycle 1 or 2, Pt agglomerates in the Pt^0 state, and the species reduced at low temperature (580 K) correspond mainly to the reduction of the superficial ceria.

Fig. 3 shows the evolution of temperature-resolved XANES-H_2 spectra of Pt/A-O2-L and Pt/CA-O2-L samples. For both samples, the spectra show initially an intense white line (WL), reflecting the high vacancy in the 5d orbital of Pt atoms [20], which is characteristic of oxidized Pt. For Pt/A-O2-L the WL decreases slightly in the temperature range of 406 to 450 K, indicating that a small fraction of Pt oxide is reduced, while the main reduction of Pt oxide occurs at temperatures higher than 580 K (Fig. 3A). On the other hand, Pt/CA-O2-L (Fig. 3B) presents a sudden reduction of the WL in the temperature range of 470–490 K, which is lower than the one for the Pt/A-O2-L sample. The reduction temperatures observed in the XANES-H_2 spectra are in good agreement with the *ex situ* TPR experiments (Fig. 2).

Fig. 4 presents the EXAFS oscillations acquired under H_2:He (5:95) at 773 K for the Pt/A-H2-L and Pt/CA-H2-L catalysts as well as the corresponding magnitude of the Fourier transform with the best fit for the first average coordination shell. Table 2 shows the fit results and the parameters for Pt foil and PtO_2 for comparison. Fig. 5 presents similar set of data for these samples after cooling under H_2:He (5:95) flow at 298 K.

The data analysis of Pt/A-H2-L and Pt/CA-H2-L catalysts acquired at 298 K gave average first-shell coordination numbers (CN_{Pt-Pt}) lower than the bulk value (8.3 and 7.2, respectively) and larger Debye–Waller factors, in agreement with the formation of

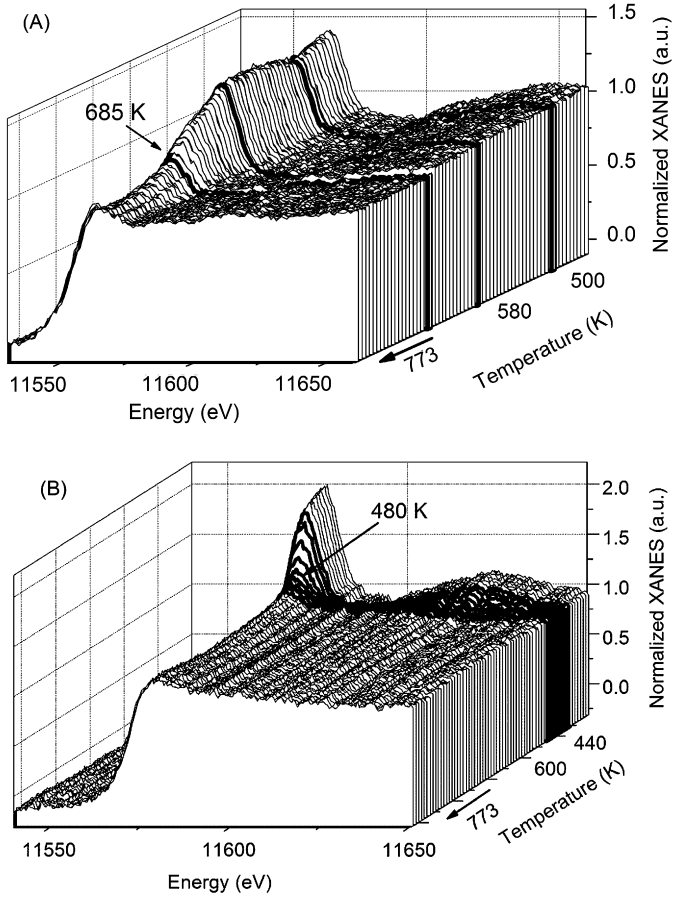

Fig. 3. Temperature-resolved XANES-H_2 for the Pt/A-O2-L (A) and Pt/CA-O2-L (B) samples, acquired during TPR at 10 K min^{-1} up to 773 K under H_2:He flow (5:95).

nanoparticles smaller than 2 nm [21,22]. Interestingly, the EXAFS data at high temperature (773 K) show that CN_{Pt-Pt} decrease compared to the data took at 298 K, for both catalysts indicating a change in the morphology of the nanoparticles. The Pt dispersion, estimated from the empirical correlation between the Pt dispersion and the average first-shell CN_{Pt-Pt} [23], is shown in Table 2. The results suggest a significant increase of Pt dispersion with the temperature increase. Pt dispersion for Pt/A-H2-L calculated from CN_{Pt-Pt} at 773 K is slightly higher than the one calculated from the data of cyclohexane dehydrogenation rate at 543 K. On the other hand, for Ce-containing catalyst (Pt/CA-H2-L) the Pt dispersion estimated from CN_{Pt-Pt} at 773 K gives a larger value. This apparent disagreement in the case of Pt/CA-H2-L between Pt dispersion estimated from CN_{Pt-Pt} and the experimental data from cyclohexane dehydrogenation could be due to the partial coverage of Pt sites by CeO_x species, suppressing the accessibility of Pt sites to cyclohexane dehydrogenation.

The Pt–Pt bond length show a strong contraction compared to the bulk (see Table 2), which is in agreement with the presence of nanoparticles [24]. It is important to remark, as shown in the literature [25–28], that the adsorption of hydrogen on Pt results in a relaxation of the Pt–Pt bond-length. However, no significant difference was found when comparing measurements at 298 and 773 K (a higher adsorption of hydrogen could be expected at 298 K). These results are attributed to the error in the Pt–Pt bond-length determination (about ±0.02 Å) in our experiments, which does not allow the observation of this effect.

A slight Pt–O scattering contribution was observed only for Pt/CA-O2-L at 773 K. The lack of a significant Pt–O scattering contribution indicates that Pt–O bonds are highly disordered for both

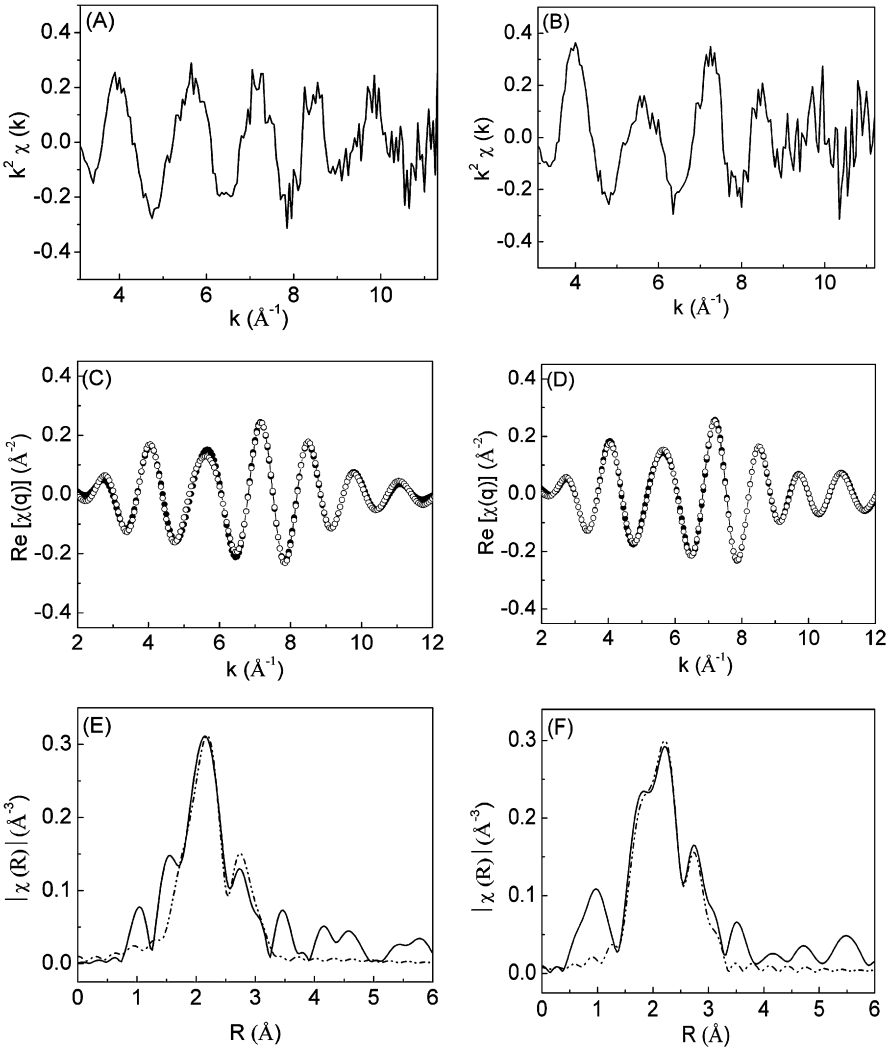

Fig. 4. EXAFS oscillations for Pt/A-H2-L (A) and Pt/CA-H2-L (B) acquired at 773 K under H_2:He (5:95) flow, the Re[$\chi(q)$] function data (C and D, respectively) and the magnitude of the Fourier transforms (E and F, respectively). The dotted lines in (E) and (F) correspond to the best fit of the first average coordination shell.

Table 2
Structural parameters obtained from EXAFS of Pt/A-H2-L and Pt/CA-H2-L catalysts under H_2 at 773 and 298 K.

Samples	Temp. of samples (K)	Scattering	CN[a]	r[a] (Å)	$\Delta\sigma^2$[a] (Å^2)	R factor	% Pt dispersion
Pt		Pt–Pt	12	2.772 ± 0.003	0.0051 ± 0.0003	–	
PtO_2[b]		Pt–O	6	1.987		–	
Pt/A-H2-L	773	Pt–Pt	5.4 ± 1.6	2.72 ± 0.03	0.012 ± 0.001	0.012	76[c] (66)[d]
Pt/A-H2-L	298	Pt–Pt	8.3 ± 1.2	2.71 ± 0.02	0.012 ± 0.001	0.009	31[c]
Pt/CA-H2-L	773	Pt–Pt	5.1 ± 0.8	2.71 ± 0.01	0.012 ± 0.001	0.003	82[c] (54)[d]
		Pt–O	0.3 ± 0.1	$2.03 + 0.02$	0.005		
Pt/CA-H2-L	298	Pt–Pt	7.2 ± 1.1	2.74 ± 0.02	0.009 ± 0.001	0.011	44[c]

[a] CN—average first shell coordination number; r—interatomic distance; $\Delta\sigma^2$—Debye–Waller factor.
[b] Theoretical values, simulated with FEFF6.
[c] Calculated from empirical correlation from CN_{Pt-Pt} at 773 K [23].
[d] Calculated from the data of cyclohexane dehydrogenation rate at 543 K [9].

catalysts, consistent with Pt nanoparticles anchorage in oxygen vacancy sites. This is in agreement with the results previously described by Kang et al. [29] for Pt/Al_2O_3 catalysts.

3.2. Catalytic test

TOF_{CH_4} analysis for steam reforming of CH_4 at 773 K, calculated from the data of cyclohexane dehydrogenation rate at 543 K, show that the TOF_{CH_4} value for Pt/CA-H2-L is about two times higher than the one found for Pt/A-H2-L (5.2 and 2.4 s^{-1}, respectively). On the other hand, Arrhenius plots for steam reforming of CH_4 show similar apparent activation energies (E_a^{app}) of 71 ± 3 kJ mol^{-1}. These values of E_a^{app} for Pt/A-H2-L and Pt/CA-H2-L are in agreement with values previously reported [4] for Pt-supported catalysts. In agreement with the results reported earlier by Otsuka at al. [30], the activity of support is not relevant relative the activity of the Pt-containing catalysts.

In situ temperature-resolved XANES-POM spectra of Pt/A-H2-L and Pt/CA-H2-L samples are shown in Fig. 6. The samples were re-

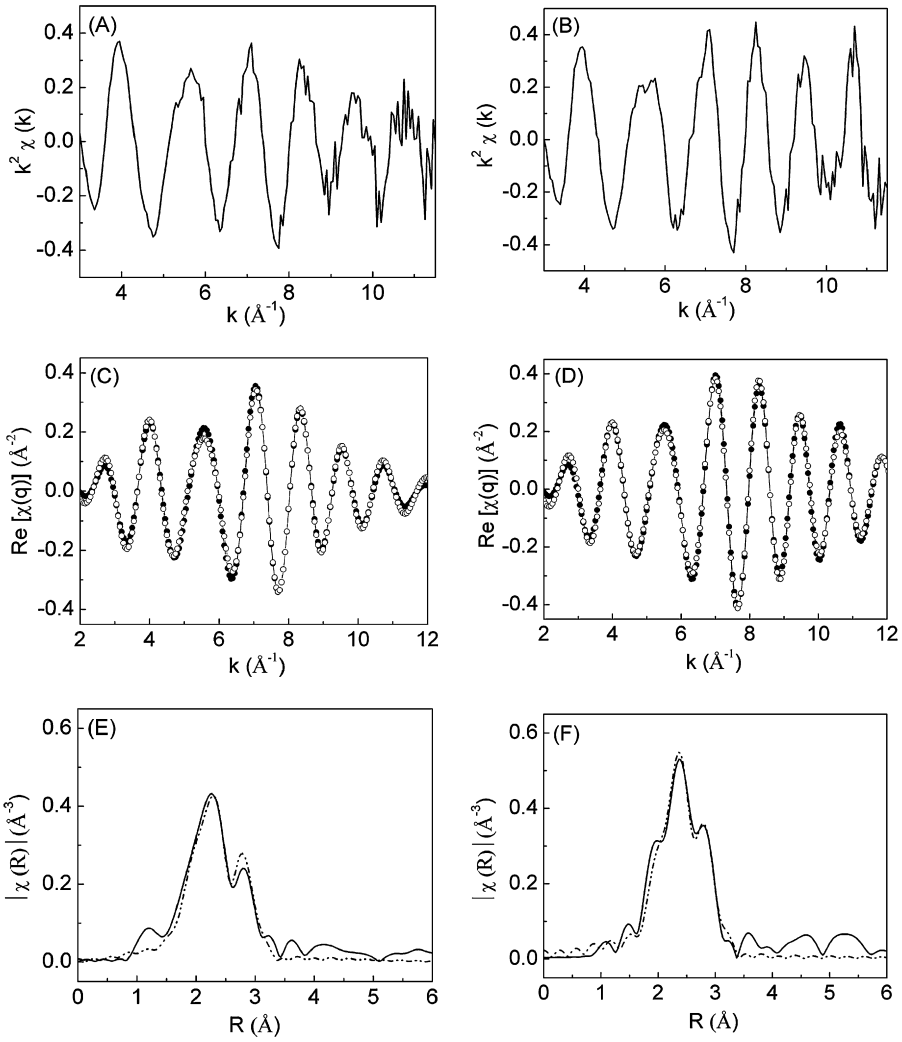

Fig. 5. EXAFS oscillations for Pt/A-H2-L (A) and Pt/CA-H2-L (B) acquired at room temperature under H_2:He (5:95) flow, the Re[$\chi(q)$] function data (C and D, respectively) and the magnitude of the Fourier transforms (E and F, respectively). The dotted lines in (E) and (F) correspond to the best fit of the first average coordination shell.

duced *in situ* and cooled down to room temperature; the H_2 flow was then replaced by a mixture for POM reaction (CH_4:O_2 = 2:1 molar). Under POM atmosphere, even at 298 K, the WL increased, indicating partial oxidation of Pt. By heating the samples under the POM mixture (Fig. 6), the WL slightly decreases at temperatures around 623 K (Pt/A-H2-L) and 673 K (Pt/CA-H2-L) and an abrupt change takes place around 735 and 725 K, respectively. It is interesting to point out that: (i) the thermal reduction of PtO_2 is expected within the region of 820–920 K; (ii) in a previous work [12], from the temperature-programmed surface reaction profile obtained for the $Pt/Ce_{0.75}Zr_{0.25}O_2$ catalyst, we demonstrated that the activation of methane occurs around 643 K and the consumption of CH_4 and O_2 was observed along with the formation of H_2O and CO_2; and (iii) above 723 K, large CH_4 consumption was detected with formation of H_2 and CO. From these results, it is reasonable to propose that the abrupt decrease in the WL at 725 K is likely due to the decomposition of CH_4 and reduction of the PtO_2 species, which occurs at similar temperatures for both Pt/A-H2-L and Pt/CA-H2-L samples.

The stability test for Pt/A-H2-L and Pt/CA-H2-L as a function of time on stream, under reaction mixtures containing various compositions (H_2O:O_2:CH_4), are shown in Fig. 7 (Pt/A-H2-L: A, d and e; Pt/CA-H2-L: A, a–c). It is clear that CeO_2-containing catalyst show higher stability (Fig. 7A, a–c), while Pt/A-H2-L catalyst showed strong deactivation under POM conditions (CH_4 conversion decreased from 64 to 27%).

The increase of the H_2O/CH_4 molar ratio in the feed leads to the increase of CH_4 conversion and increase of H_2/CO molar ratio, shown in Fig. 7B for Pt/CA-H2-L. Similar effect was verified for Pd/CeO_2–Al_2O_3 catalysts [31]. This fact has been attributed to the occurrence of steam reforming of CH_4 (SRM). Therefore, the increase in the activity can be attributed to the ability of H_2O to gasify carbon active on metal surface [6]. On the other hand, an improvement of the heat transfer coefficient due to the increase of the H_2O contents in the feed should also be considered.

Fig. 8 shows TEM images of Pt/A-O2-L (Fig. 8A) and Pt/CA-O2-L (Fig. 8D), Pt/A-H2-L (Fig. 8B) and Pt/CA-H2-L (Fig. 8E), and Pt/A-H2-L (Fig. 8C) and Pt/CA-H2-L (Fig. 8F) after ATR reaction (H_2O:O_2:CH_4 of 0.65:2:1 at 1073 K during 24 h on stream). The presence of the support, particularly for the Pt/CA samples, makes it difficult to obtain a good estimate of the Pt size distribution. But it is clear from the TEM images that the particles are very small, in agreement with the cyclohexane dehydrogenation results and EXAFS analysis. Only after ATR reaction, in the case of the Pt/A-H2-L sample, an extensive growth of the Pt nanoparticles can be easily identified. In addition, the alumina support also modifies significantly after reaction (Fig. 8C), while the ceria–alumina support does not (Fig. 8F).

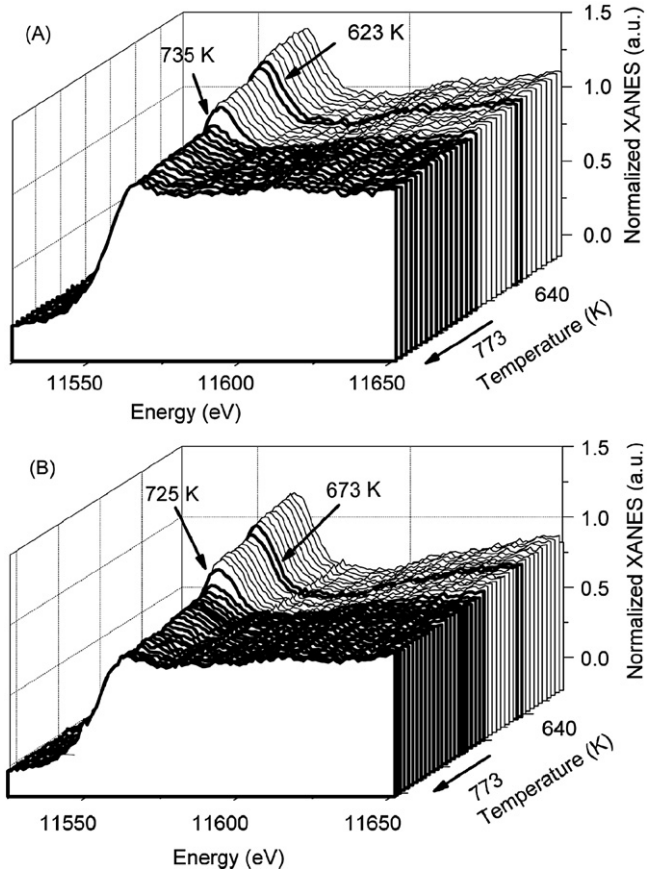

Fig. 6. Temperature-resolved XANES-POM for the Pt/A-H2-L (A) and Pt/CA-H2-L (B) catalysts. After *in situ* reduction, the H_2 was replaced by the POM mixture (CH_4:O_2 = 2:1 v:v) at 298 K. The spectra were acquired during heating at 10 K min^{-1} up to 973 K, under 100 mL min^{-1} of POM mixture.

High resolution TEM images of the reduced catalysts before and after ATR reaction (reduced and spent catalysts) are shown in Fig. 9. It can be seen from the lattice fringes that both catalysts show well crystallized metallic Pt particles after reduction (Fig. 9A and B). After ATR reaction, however, the nanoparticles in the spent Pt/A-H2-L catalyst grow and become facetted (Fig. 9B). On the other hand, the Pt nanoparticles do not show significant modification in the case of the Pt/CA-H2-L catalyst.

4. Discussion

The analysis of the Pt/A and Pt/CA catalysts showed some interesting results that contribute to understand the differences in catalytic performance in ATR and POM reactions. The quantitative analysis of the EXAFS oscillations showed reduction of the CN_{Pt-Pt},

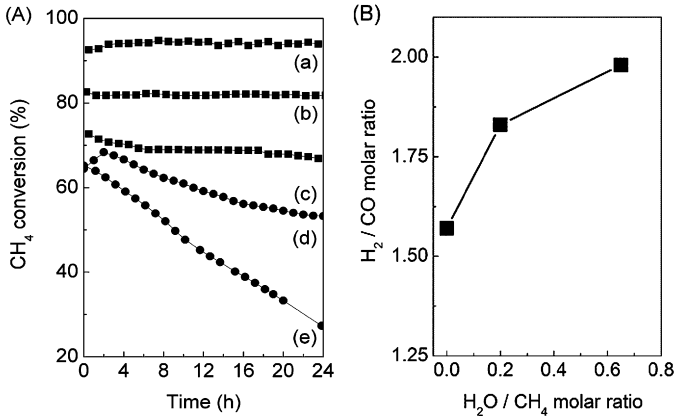

Fig. 7. CH_4 conversion with time on stream for Pt/A-H2-L (A, d and e) and Pt/CA-H2-L (A, a–c) catalysts under various feed compositions (H_2O:O_2:CH_4) at 1073 K and corresponding H_2/CO molar ratio for the Pt/CA-H2-L catalyst (B). Feed composition (H_2O:O_2:CH_4): (a, d) 0.65:0.5:1.0, (b) 0.2:0.5:1.0, and (c, e) 0.0:0.5:1.0.

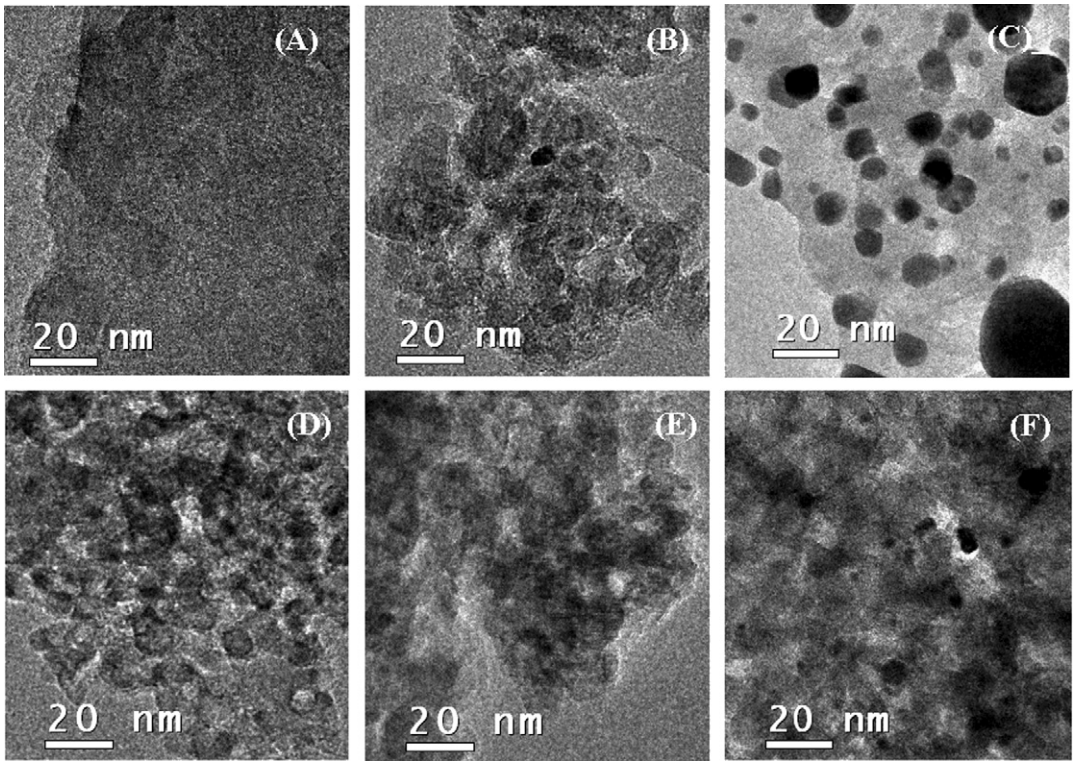

Fig. 8. TEM images: Pt/A-O2-L (A), Pt/A-H2-L (B) and Pt/A-H2-L after ATR reaction (C); Pt/CA-O2-L (D), Pt/CA-H2-L (E) and Pt/CA-H2-L after ATR reaction (F). ATR conditions: H_2O:O_2:CH_4 = 0.65:0.5:1, 1073 K for 24 h.

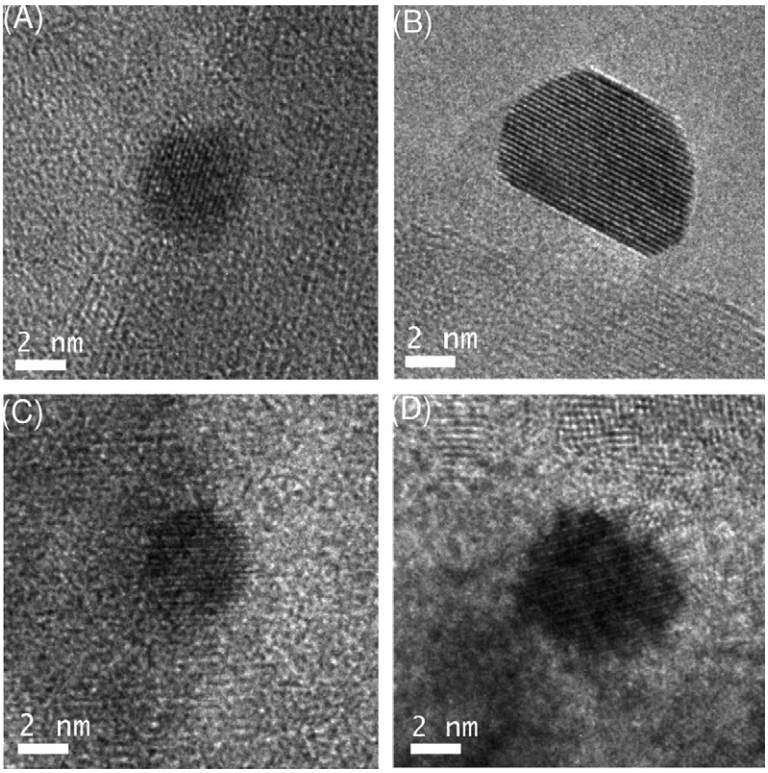

Fig. 9. HRTEM images of the Pt/A-H2-L (A) after ATR reaction (B); Pt/CA-H2-L (C) and after ATR reaction (D). ATR conditions: $H_2O{:}O_2{:}CH_4 = 0.65{:}0.5{:}1$, 1073 K for 24 h.

contraction of the interatomic distance, and increase of the Debye–Waller factor, when compared to the bulk Pt values, in agreement with the formation of very small nanoparticles (<2 nm) [22,24]. The dehybridization of the *spd* metal orbitals may result in an increase of local electron density between atoms in small particles, and a contraction of the interatomic Pt–Pt distance. This effect leads to a larger disorder, which is reflected in a larger Debye–Waller factor [27].

The Pt particle sizes were similar in both Pt/A-H2-L and Pt/CA-H2-L catalysts. By comparing the analysis at 298 and 773 K, there is a significant reduction of the CN_{Pt-Pt}, suggesting a change in particle morphology (flattening), which was similar for both catalysts. The flattening of the Pt particles onto the support correspond to a new surface energy balance, which could be caused either by desorption of the H* or by the increase of the temperature, and would supposedly be compensated by the increase of the interaction between the Pt and the oxygen from the support. It is well known that for Pt on different supports, the desorption of hydrogen leads to a decrease of CN_{Pt-Pt} [24,27]. This change is smaller than the one observed for Pt/A-H and Pt/CA-H catalysts when the temperature increases from 298 to 773 K. Considering that the EXAFS spectra were performed under H_2 flow at 298 and 773 K and the adsorption of H_2 is in equilibrium, then it is reasonable to expect that the changes observed in CN_{Pt-Pt} are mainly due the thermal effects.

These results stress the differences that maybe be found by various techniques. For example, the properties of Pt particles measured by adsorption techniques at low temperatures are different from the ones obtained under reforming reaction conditions. The comparison with cyclohexane hydrogenation results in this work also confirms that part of the Pt sites is covered by CeO_x species. Based on that, we believe that a more realistic number of Pt atoms on the surface is better obtained from Pt dispersion estimated by cyclohexane dehydrogenation at 543 K. This temperature is closer to the one used in the steam reforming in this study (773 K) and may better reflect the differences when using mixed-oxide supports.

Considering the catalytic results, the Pt/CA-H2-L catalysts exhibit higher TOF_{CH_4} for steam reforming of CH_4. We should point out that: (i) TOF_{CH_4} for steam reforming of methane increases significantly with increasing Pt dispersion [4], and an increase of local electron density is expected with increasing metal dispersion [32]; (ii) the similar Pt dispersions estimated from CN_{Pt-Pt} and interatomic Pt–Pt distance for Pt/A-H2-L and Pt/CA-H2-L catalysts indicate similar local electron density of Pt in both catalysts; (iii) the similar values of E_a^{app} of 73 ± 3 kJ mol^{-1} obtained for steam reforming of methane are also in agreement with these results. Then, similar TOF_{CH_4} in steam reforming would be expected for both the Pt/A-H2-L and Pt/CA-H2-L catalysts. However, this was not the case.

In order to understand these activity results, we should consider the FTIR of adsorbed CO data on Pt/CA-H2-L and Pt/A-H2-L catalysts, reported in an earlier paper [32], which suggest a partial coverage of Pt particles by CeO_x species in the Pt/CA-H2-L catalyst. This was also confirmed by the comparison of EXAFS and cyclohexane dehydrogenation results. Another aspect to consider is the mechanism for steam reforming of methane [3,4,6], where CH_4 decomposes to form chemisorbed carbon (C*). The active C* on the metal surface can be removed by reaction with surface oxygen (O*) to produce CO. As demonstrated previously by Wei and Iglesia [6], the amount of C* on the surface depends on the amount of O* available for the reaction $C^* + O^* \leftrightarrow CO$. Similar to what was previously proposed for Pd/CeO_2–Al_2O_3 catalysts in steam reforming of methane [10,30], the aduct Pt[CeO_x] species onto Pt surface may be oxidized by H_2O or CO_2 and transfer O* to oxidize the C* deposited on Pt surface, restoring Pt[CeO_x] species. Consequently, the lower capacity to transfer O* in the Pt/A-H2-L catalyst results in higher blocking of Pt sites by carbon, which leads to a lower accessibility of the active sites to CH_4 and consequently to lower TOF_{CH_4} than that in the Pt/CA-H2-L catalyst. The higher susceptibly to carbon

deposition on Pt/A catalysts used in POM was previously verified by TEM analysis [11].

Another important result showed by TPR, XRD and TEM is the stability of the Pt nanoparticles, submitted to different reduction–oxidation cycles. The results clearly show that treatment in presence of O_2 at 1073 K leads to Pt agglomeration. On the other hand, Pt particles under H_2 are quite stable at same temperature. These results are consistent with the high energy required to break Pt–Pt bonds to transfer Pt to the vapor phase and allow the growth of Pt particles. The high stability of Pt particles in Pt/A-H2-H and Pt/CA-H2-H also suggest high stability of the support under H_2, which suppress cluster growth by coalescence or migration along the surface. Different from Pt, PtO_2 has low sublimation energy and can be an intermediate species either for surface diffusion or vapor phase transport [34], resulting in the growth of Pt clusters in oxidizing atmosphere.

The standard free energy of formation of PtO_2 [$O_2(g) + Pt^0(s) \leftrightarrow PtO_2(s)$] depends on the Pt-cluster curvature [35], and the free energy decreases with decreasing Pt-cluster sizes. Then, PtO_2 formation will be favored at low temperatures in small Pt-nanoparticles, but not in large ones. Temperature-resolved XANES-POM spectra for Pt/A-H2-L and Pt/CA-H2-L show a strong oxidation of Pt at low temperature when the catalysts are exposed to the POM mixture at 298 K. This is in agreement with the presence of small Pt nanoparticles. The temperature-resolved XANES-POM spectra pointed out that the Pt oxidized at low temperature is re-reduced by increasing the temperature above ~700 K. The fact that Pt oxide species are reduced at low temperatures, for both Pt/A-H2-L and Pt/CA-H2-L, under a mixture of $CH_4{:}O_2 = 2{:}1$, suggests a very small concentration of remaining Pt oxide species in conditions of POM or ATR at high temperature (1073 K). This is an important result since the growth of the Pt clusters by PtO_2 surface diffusion or vapor phase transport is then suppressed [34].

It is interesting to consider that: (i) the reduction temperatures under POM condition are lower than the ones expect for a thermal reduction, and at a low temperature, around 730 K, the Pt growth by surface diffusion and vapor phase transport of PtO_x species would be not important; (ii) both Pt/A-H2-H and Pt/CA-H2-H catalysts show high stability, and (iii) both catalysts exhibit similar Pt particle size. From these results and considerations, it is reasonable to expected similar stability for Pt/A-H2-L and Pt/CA-H2-L in ATR or POM reactions at 1073 K. However, TEM images reveal a strong growth of Pt particles for Pt/A-H2-L catalyst used in ATR reaction for 24 h at 1073 K, resulting in strong deactivation. In contrast, Pt particles in Pt/CA-H2-L catalysts were quite stable.

In fact, TEM images of ATR spent catalysts also show better stability of the ceria-alumina support when compared to alumina only. There is a clear change in the morphology of the Al_2O_3 support (Fig. 8C), whereas the Ce-containing support was highly stable (Fig. 8F). This effect can contribute significantly to the mobility of Pt clusters, resulting in the strong coalescence of Pt in our Pt/A-H2-L catalyst.

The high stability of Pt in Ce-containing supports, under oxidizing conditions at high temperature, have been assigned to Pt–O–Ce bond, which act as an anchor and inhibit the sintering of Pt [8]. In fact, EXAFS results showed a slightly higher Pt–O scattering contribution for the Pt/CA-H2-L catalyst under H_2 at 773 K and the FTIR of adsorbed CO showed suppression of the CO linearly adsorbed on Pt/CA catalysts [33]. The evidence of the Pt-CeO_x interaction should be considered to explain the higher activity and stability of Pt under oxidizing condition. This Pt–CeO_x species can act as an anchor to avoid the sublimation of the PtO_2 and to transfer O^* to Pt sites with oxidation of carbon on its surface, resulting in higher activity catalysts for reforming of methane and higher resistance to carbon deposition on Pt/CA-H2-L catalyst in POM or ATR.

5. Conclusions

In this work, we report some interesting findings that should contribute to the understanding of the differences in catalytic performance of Pt supported on alumina and ceria-alumina (Pt/A and Pt/CA) in autothermal reforming and the partial oxidation of methane (ATR and POM). It is found that the presence of ceria decreases the density of available Pt sites, but it leads to higher accessibility of the active sites to CH_4 and higher TOF for the steam reforming of CH_4.

The main conclusions of the study are as follows:

(1) The interaction of reduced Pt and Ce oxide in the presence of O_2 inhibits Pt sintering by surface diffusion. The high thermal stability of the Ce-containing support and its ability to anchor metallic Pt nanoparticles helps in the retention of surface area and prevents the migration and coalescence of the metal crystallites.
(2) Pt is reduced by CH_4 in the presence of O_2 in the ATR or POM reactions, decreasing the PtO_2 content. Pt is predominantly in a reduced state, which suppresses sintering via the formation of mobile and volatile PtO_2.

Acknowledgments

The authors are grateful for the financial support of CNPq (Conselho Nacional de Desenvolvimento Cientifico e Tecnológico) and PETROBRAS (0050.0007696.04.2). The Brazilian Synchrotron Light Laboratory (LNLS) is acknowledged for the use of its facilities and technical support in TEM (LME) and XAFS (DXAS and XAFS2 beamline) experiments.

References

[1] P.K. Bakkerud, Catal. Today 106 (2005) 30.
[2] K. Aasberg-Petersen, T.S. Christensen, C.S. Nielsen, I. Dybkjaer, Fuel Process. Technol. 83 (2003) 253.
[3] G. Jones, J.G. Jakobsen, S.S. Shim, J. Kleisa, M.P. Andersson, J. Rossmeisl, F. Abild-Pedersen, T. Bligaard, S. Helvegc, B. Hinnemann, J.R. Rostrup-Nielsen, I. Chorkendorff, J. Sehested, J.K. Nørskova, J. Catal. 259 (2008) 147.
[4] J. Wei, E. Iglesia, J. Phys. Chem. B 108 (2004) 4094.
[5] J. Wei, E. Iglesia, J. Phys. Chem. Chem. Phys. 6 (2004) 3754.
[6] J. Wei, E. Iglesia, J. Catal. 224 (2004) 370.
[7] E. Becker, Per-Anders Carlsson, H. Grönbeck, M. Skoglundh, J. Catal. 252 (2007) 11.
[8] Y. Nagai, T. Hirabayashi, K. Dohmae, N. Takai, T. Minami, H. Shinjoh, S. Matsumoto, J. Catal. 242 (2006) 103.
[9] A.C.S.F. Santos, S. Damyanova, G.N.R. Teixeira, L.V. Mattos, F.B. Noronha, F.B. Passos, J.M.C. Bueno, Appl. Catal. A Gen. 290 (2005) 123.
[10] L.S.F. Feio, C.E. Hori, S. Damyanova, F.B. Noronha, W.H. Cassinelli, C.M.P. Marques, J.M.C. Bueno, Appl. Catal. A Gen. 316 (2007) 107.
[11] J.C.S. Araujo, D. Zanchet, R. Rinaldi, U. Schuchardt, C.E. Hori, J.L.G. Fierro, J.M.C. Bueno, Appl. Catal. B 84 (2008) 552.
[12] J.A.C. Ruiz, F.B. Passos, J.M.C. Bueno, E.F. Souza-Aguiar, L.V. Mattos, F.B. Noronha, Appl. Catal. A Gen. 334 (2008) 259.
[13] S. Damyanova, J.M.C. Bueno, Appl. Catal. A Gen. 253 (2003) 135.
[14] B.L. Mojet, M.S. Hoogenraad, A.J. Van Dillen, J.W. Geus, D.C. Koningsberger, J. Chem. Soc. Faraday Trans. 93 (24) (1997) 4371.
[15] D.C. Koningsberger, in: J. Baruchel, J.L. Hodeau, M.S. Lehmann, J.R. Regnard, C. Schlenker (Eds.), Applications to Solid State Physics and Chemistry, Neutron and Synchrotron Radiation for Condensed Matter Studies, vol. II, Springer, Berlin, 1994, p. 213.
[16] H. Lieske, G. Lietz, H. Spindler, J. Völter, J. Catal. 81 (1983) 8; H.C. Yao, Y.F.Y. Yao, J. Catal. 86 (1984) 254.
[17] A. Piras, A. Trovarelli, G. Dolcetti, Appl. Catal. B Environ. 28 (2000) L77.
[18] S. Damyanova, C.A. Perez, M. Schmal, J.M.C. Bueno, Appl. Catal. A Gen. 234 (2002) 271.
[19] A.I. Kozlov, D.H. Kim, A. Yezerets, P. Andersen, H.H. Kung, M.C. Kung, J. Catal. 209 (2002) 417.
[20] M. Brown, R. Pieierls, E. Stern, Phys. Rev. B 15 (1977) 738.
[21] B. Shelimov, J.-F. Lambert, M. Che, B. Didillon, J. Catal. 185 (1999) 462.
[22] J.M. Ramallo-López, F.G. Riquejo, A.F. Craievich, J. Wei, M. Avalos-Borjad, E. Iglesia, J. Mol. Catal. A 228 (2005) 299.

[23] J.T. Miller, A.J. Kropf, Y. Zha, J.R. Regalbuto, L. Delannoy, C. Louis, E. Bus, J.A. van Bokhoven, J. Catal. 240 (2006) 222.
[24] A.I. Frenkel, C.W. Hills, R.G. Nuzzo, J. Phys. Chem. B 105 (2001) 12691.
[25] F.W. Lytle, R.B. Greegor, E.C. Marques, D.R. Sandstrom, G.H. Via, J.H. Sinfelt, J. Catal. 95 (1985) 546.
[26] B. Hammer, J.K. Nørskov, Nature 376 (1995) 238.
[27] A.Yu. Stakheev, Y. Zhang, A.V. Ivanov, G.N. Baeva, D.E. Ramaker, D.C. Koningsberger, J. Phys. Chem. C 111 (2007) 3938.
[28] S.N. Reifsnyder, M.M. Otten, D.E. Sayers, H.H. Lamb, J. Phys. Chem. B 101 (1997) 4972.
[29] J.H. Kang, L.D. Menard, R.G. Nuzzo, A.I. Frenkel, J. Am. Chem. Soc. 128 (2006) 12068.
[30] K. Otsuka, Y. Wang, E. Sunada, I. Yamanaka, J. Catal. 175 (1998) 152.
[31] L.S.F. Feio, C.E. Hori, L.V. Mattos, D. Zanchet, F.B. Noronha, J.M.C. Bueno, Appl. Catal. A 348 (2008) 183.
[32] D. Bazin, D. Sayers, J.J. Rehr, C. Matteri, J. Phys. Chem. B 101 (1997) 5332.
[33] B.A. Riguetto, S. Damyanova, G. Gouliev, C.M.P. Marques, A. Petrov, J.M.C. Bueno, J. Phys. Chem. B 108 (2004) 5349.
[34] P. Wyblatt, Acta Metall. 24 (1976) 1175.
[35] X. Lai, D.W. Goodman, J. Mol. Catal. A Chem. 162 (2000) 33.